PHYSICAL REVIEW E **66**, 051603 (2002)

Interface scaling in a two-dimensional porous medium under combined viscous, gravity, and capillary effects

Yves Méheust,[1,2] Grunde Løvoll,[2,1] Knut Jørgen Måløy,[2] and Jean Schmittbuhl[1]
[1]*Laboratoire de Géologie, École Normale Supérieure, Paris, France*
[2]*Department of Physics, University of Oslo, Oslo, Norway*

(Received 6 July 2001; published 11 November 2002)

We have investigated experimentally the competition between viscous, capillary, and gravity forces during drainage in a two-dimensional synthetic porous medium. The displacement of a mixture of glycerol and water by air at constant withdrawal rate has been studied. The setup can be tilted to tune gravity, and pressure is recorded at the outlet of the model. Viscous forces tend to destabilize the displacement front into narrow fingers against the stabilizing effect of gravity. Subsequently, a viscous instability is observed for sufficiently large withdrawal speeds or sufficiently low gravity components on the model. We predict the scaling of the front width for stable situations and characterize it experimentally through analyses of the invasion front geometry and pressure recordings. The front width under stable displacement and the threshold for the instability are shown, both experimentally and theoretically, to be controlled by a dimensionless number F which is defined as the ratio of the effective fluid pressure drop (i.e., average hydrostatic pressure drop minus viscous pressure drop) at pore scale to the width of the fluctuations in the threshold capillary pressures.

DOI: 10.1103/PhysRevE.66.051603 PACS number(s): 47.55.Mh, 47.20.Gv, 68.05.Cf, 47.53.+n

I. INTRODUCTION

Multiphase fluid flows in porous media have many important applications in geological engineering, including ground water flow modeling and oil recovery, where an increase in the recovery rate is obtained by injection of another fluid phase [1–8]. In immiscible two phase flows, strong variations exist in the obtained displacement structures and dynamics, depending on the flow rates, wetting properties, viscosity ratios, and density differences of the involved fluids [9,10].

If one considers situations in which a nonwetting fluid invades a porous medium saturated with a wetting fluid (drainage) with a higher viscosity, in the absence of gravity, two regimes can be distinguished. At very low flow rates, the viscous pressure drop across the porous medium is negligible in comparison to the inhomogeneity in the threshold capillary pressures inside the medium. The topology of the random porous medium causes the fluctuations in the pressure field needed for the nonwetting phase to invade new pores. The resulting displacement structure is controlled by capillary effects, and is well described by the invasion percolation algorithm. This *capillary fingering regime* has been studied extensively [11–13]. At high flow rates, viscous forces dominate capillary and gravitational effects. The displacement is stable or unstable depending on which phase is the most viscous [4,14–16]. If the defending phase is the most viscous one, the displacement is unstable [4,14,17,18]. This *viscous fingering regime* has strong analogies to diffusion-limited aggregation (DLA) patterns [19–23]. In the opposite case in which the invading fluid is the most viscous one, viscous effects stabilize the front [16,24].

However, most real reservoir systems are not flat and horizontal, and are therefore sensitive to gravity effects. If the two fluids involved have different densities, gravity forces modify the displacement structure dramatically [25–28]. Gravity causes hydrostatic pressure gradients that might stabilize or destabilize fluid motion.

In the capillary fingering regime, stabilization of the fluid interface by gravity has been studied both theoretically and experimentally in two and three dimensional media [25,26,29,30]. Unstable buoyancy driven migration of a lighter fluid into a denser one has also been studied by use of experiments, computer simulations and theoretically [27,28,31–33]. All these studies of gravitational effects concentrate on situations where the flow rates are so low that capillary forces are large compared to viscous forces at pore scale. For such systems the obtained flow patterns are understood in terms of the competition between gravity forces and local nonhomogeneous capillary forces [25,26]. It should be noted that though the obtained displacement patterns could be modeled without considering viscosity, viscous effects have to be taken into account to understand the local dynamics during invasion [34,35].

The competition between gravity and viscous forces has been studied for immiscible flows in a Hele-Shaw cell without any porous medium. Saffman and Taylor have studied small perturbations of the displacement front, deriving a criterion for the instability [36]; but it is not obvious that the arguments developed for this particular geometry apply to flows in porous media, where the complexity of the flow boundary conditions plays a crucial role [17]. The deformation and breakup of nonwetting clusters by a viscous pressure field has also been studied for a system without gravity effects [37]. Situations where all three forces are significant have been studied for imbibition in a sand pack [38], with a focus on the saturation of the nonwetting fluid, and for simulations of viscous fingering in a gravity field, at reservoir scale [7,39].

The purpose of this work is to address the scaling properties of an interface during a two phase flow in a porous medium when capillary, gravity and viscous forces play a comparable role. We have studied specifically the stabiliza-

1063-651X/2002/66(5)/051603(12)/$20.00

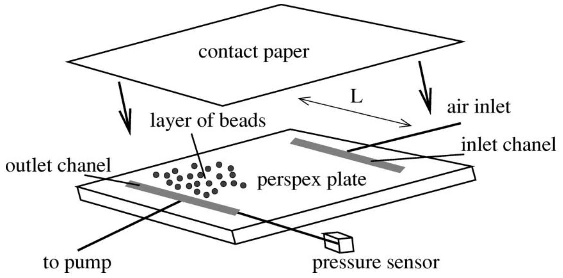

FIG. 1. Sketch of the two-dimensional porous medium used in the experiments. The beads are 1 mm in diameter and the distance between the channels is $L=350$ mm. The model is sealed with silicone glue along the edges. The size of the model is $L\times L$.

tion and destabilization of the displacement front obtained by injection of air from above in a two dimensional porous medium saturated with a wetting fluid. This system was studied systematically by tuning gravity and viscous forces: the gravitational component on the model could be varied by tilting the model at different angles, while the magnitude of viscous forces could be changed by varying the injection rate, which was typically high enough for viscous fingering to occur at low inclination angles.

The present article is organized as follows. The experimental setup and the methods used for treating the data are described and discussed in Sec. II. In Sec. III, we discuss the competition between gravity forces, viscous forces and capillary forces from a theoretical point of view. The experimental results are presented in Sec. IV, which is followed by a discussion of the results in Sec. IV E and some concluding remarks in Sec. V.

II. EXPERIMENTAL METHOD

A. Experimental setup and procedure

The model used in the study is similar to the one used in [14,15] and [37]. A two dimensional porous media is made by pouring glass beads of diameter $a=1$ mm on the sticky side of a 500×500 mm^2 contact paper until no more beads stick to the surface. The excess beads are then removed so that the resulting porous matrix is a random monolayer of beads. The contact paper is glued to a Plexiglas plate with milled in and outlet channels. The channels are parallel and separated by 350 mm. They are 5 mm wide, 8 mm deep and 350 mm long, which makes the size of the porous medium $L\times L$, with $L=350$ mm. When the model is installed, the outlet channel is connected to a pump and a *Honeywell 26PCA Flow-Through* pressure sensor. The channels are cut open and the edges of the model are sealed and constrained with silicone glue. Then another sheet of contact paper is glued on top of the beads so as to make a ‘‘sandwich’’ (see Fig. 1). The model is then placed (beads down) on top of another Plexiglas plate with a ‘‘pressure cushion’’ to ensure that the model is kept in position and that it is always only one bead diameter thick. The porosity ϕ of the model is measured to be 0.63 and the permeability κ is measured to be $\kappa=0.0189\times10^{-3}$ cm$^2=1948$ darcy.

The defending wetting fluid used in all our experiments is a 90–10 % by weight *glycerol-water* solution dyed with 0.1% Negrosine. *Air* is used as the invading nonwetting fluid. The *wetting* glycerol-water solution has a viscosity of $\mu_w\approx0.2$ Pa s and a density of $\rho_w=1235$ kg m^{-3} at room temperature. The corresponding parameters for the *nonwetting* air are $\mu_{nw}=1.9\times10^{-5}$ Pa s and $\rho_{nw}=116$ kg m^{-3}. The surface tension between these two liquids σ is 6.4×10^{-2} N m^{-1}. The temperature in the defending fluid is measured at the outlet of the model during each experiment to be able to estimate the viscosity. A ±1 °C uncertainty between this measured value and the temperature of the fluid inside the model is assumed, resulting in a $\pm2\times10^{-2}$ Pa s uncertainty in the estimated viscosity.

To get stable flow out of the model we use gravity to pump the defending fluid out of the model. This is done by leading the fluid out of the model and down to a reservoir on the floor below ($\sim$4 m height difference). The flow rate is controlled by a valve and measured during experiments with an electronic scale. Flow rate variations during an experiment are always smaller than 3% of Q.

The *Honeywell 26PCA Flow-Through* pressure sensor measures the pressure in the outlet channel during experiments. By using the pressure in the outlet channel at breakthrough as a reference, we measure the pressure difference between the invasion front and the outlet channel during the experiment.

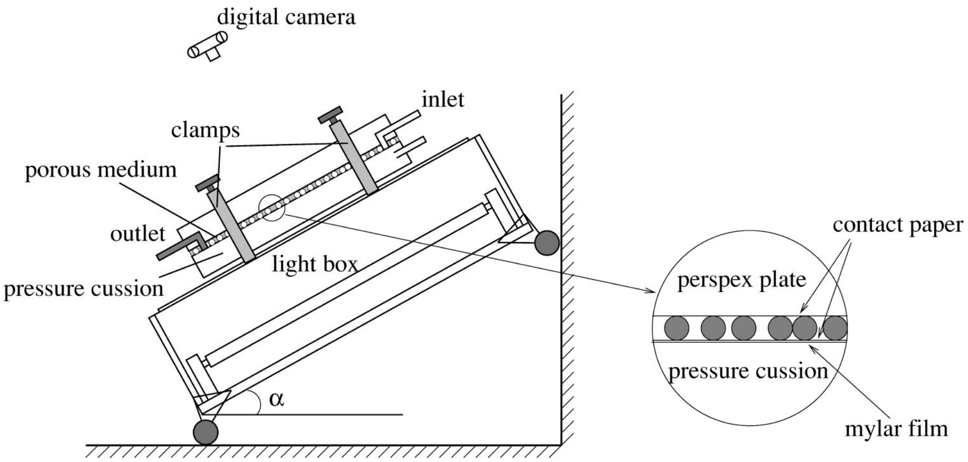

FIG. 2. Sketch of the experimental setup. The gravity component on the porous medium is varied by changing the tilt angle of the setup.

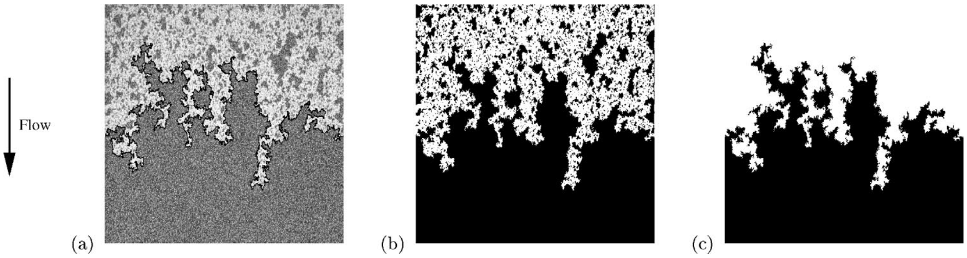

FIG. 3. (a) Comparison between the original picture of the flow structure and the extracted invasion front. The whole model (35×35 cm^2) is represented. The withdrawal rate is 1.5 ml min^{-1}. The inclination angle is 20.3° (experiment 38). This situation corresponds to an intermediate regime in which a significant viscosity-related fingering exists at some places in the displacement structure, while other parts of it exhibit a dynamics closer to capillary fingering. Anisotropic shapes of the interface and the trapped clusters are the signature of this crossover regime. (b) Corresponding extracted black and white picture. The displacement structure appears white. Its aspect is related to the physical phenomena occurring during drainage. (c) Black and white picture after removal of the trapped clusters. The front plotted in (a) on top of the raw image has been obtained as the line separating the white from the black area in (c).

The model is clamped to a light box that can be tilted to various inclination angles to vary the component of gravity on the porous medium. The component of gravity along the model g is given by $g = g_0 \sin(\alpha)$, where g_0 is the acceleration of gravity and α is the inclination angle (see Fig. 2). The pressure drop between the outlet of the model and the reservoir is much larger than that between the inlet and the outlet of the model. The flow rate is therefore controlled by the former pressure drop, and its dependence on the tilting of the experimental setup or on the volume of wetting fluid inside the model is very weak. Thus, gravity can be considered to be tuned independently of the flow rate.

The displacement structure is visualized by illuminating the model with the light box and taking pictures with an attached *Kodak DCS 420 CCD* camera, which is controlled by a computer over a SCSI connection. Pictures are taken at regular time intervals during fluid displacement. They have a resolution of 1536×1024 pixels, with 8 bits gray levels, which provides a spatial resolution of 0.37 mm per pixel or ~ 2.56 pixels per pore.

B. Image treatment

1. Front extraction

The raw images display a variety of gray scales. A region with very light gray shadings corresponding to air and others with dark shadings corresponding to dyed glycerol [see Fig. 3(a)] can be distinguished. Glass beads appear as medium gray spots randomly distributed in the picture. In order to extract the part of the model that is filled with air, all gray levels below a given threshold are set to black, while the others are set to white. The threshold chosen varies along the direction normal to the direction of drainage, to account for the enlightenment nonuniformity. During this thresholding process, glass beads are arbitrarily determined to be part of the white or of the black region. This does not affect the accuracy of the following analyses, since only scales larger than the typical pore size, a, are considered as significant. Geometrical information about the drainage process contained in the raw picture is passed to the resulting black and white picture [see Fig. 3(b)]. We call the white region in this picture *displacement structure*. Apart from included glass beads, it corresponds to the part of the model filled with air.

The black islands inside the white area in the black and white picture are *clusters* of wetting fluid that have been trapped in air during drainage, as two neighboring fingers of the fronts advancing ahead of the rest of the front have merged. Removal of the trapped clusters is achieved by painting white all black islands in the picture except the largest one, leaving only one continuous white area and one continuous black area [see Fig. 3(c)]. The latter is then separated from the former by a continuous line, the *displacement front*, which is the limit for the penetration of air inside glycerol. In what follows, we often simply call it *the front*. In Fig. 3(a), the front is shown in black on top of the raw image. Visual inspection shows a very good consistency between the raw image and the extracted front.

The spatial resolution in our setup allows us to observe geometrical features for all scales down to pore scale, a.

2. Front analysis

The front is analyzed in terms of vertical extension, and statistical geometrical properties (using the two-point correlation function and the box counting method).

The descending coordinate along the maximum slope of the model is denoted z, the horizontal direction normal to z is called x. The frame (x,z) defines positions inside the model. Some of these positions, denoted $\boldsymbol{r}_i = (x_i, z_i)$, correspond to points that belong to the front. From the knowledge of these points, we define the following characteristic quantities for the front: its maximal extension along z, Δz, its width, w, defined as the root mean square of the z_i distribution, and the two-point correlation function $C(s)$, s being the scale of observation:

$$C(s) = \langle\langle \Theta(\boldsymbol{r}_0)\Theta(\boldsymbol{r}_0 + \boldsymbol{s})\rangle\rangle_{|\boldsymbol{s}|=s}, \qquad (1)$$

where $\boldsymbol{r}_0$ is a point on the front and $\boldsymbol{s}$ is a vector from this point. $\Theta(\boldsymbol{r})$ is 1 for points on the front and 0 otherwise. The double average denotes an average over all $\boldsymbol{r}_0$ on the front and all possible directions of $\boldsymbol{s}$. For a fractal front with a fractal dimension D, it has been shown [40] that $C(s)$ is a power law of the scale s with an exponent $2-D$. We also define the number N_s of square boxes of side length s that are required for entirely covering the front. For a fractal front with a fractal dimension D, this box-counting method provides a power law with an exponent $-D$ [41].

III. COMPETITION BETWEEN GRAVITY AND VISCOUS FORCES

When one fluid invades another fluid with a different density, gravity forces tend to either stabilize or destabilize fluid displacement, depending on the density differences and flow directions [25,27,28,33,42]. We focus here on a situation where a less dense fluid with a negligible viscosity displaces a denser viscous fluid from above. In this case, the hydrostatic pressure gradient tends to annihilate any height difference between two points along the front, while local viscous effects tend to promote any part of the front that is progressing faster than the rest of it. The influence of gravity on the displacement structure depends both upon the gravity component on the model and upon the relative magnitudes of capillary and viscous forces.

The latter relative magnitudes are usually quantified by use of the capillary number C_a, which denominates the ratio of viscous forces to capillary forces at pore level:

$$C_a = \frac{\mu v a^2}{\gamma \kappa}, \tag{2}$$

where μ is the viscosity of the fluid, v is the filtering or Darcy velocity in the medium, a is the typical pore size, γ is the surface tension between the two fluids and κ is the permeability of the porous medium. Various values for the capillary number give rise to different displacement structures. The limit cases, i.e., capillary fingering for $C_a \ll 1$ and viscous fingering for $C_a \gg 1$, are well known.

For displacements sufficiently slow for viscous forces to be negligible with respect to the fluctuations in threshold capillary pressures, the width of the invasion front is controlled by the latter fluctuations along the front. The dimensionless *Bond number* B_o [25–27], quantifies the competition between capillary forces and gravity at pore scale:

$$B_o = \frac{\Delta \rho g a^2}{\gamma}, \tag{3}$$

where $\Delta\rho$ is the difference in the two liquids' densities and g is the component of gravity along the direction of displacement. The front width w for these slow displacements was found to scale with the *Bond number* as $w \sim B_o^{-\nu/(1+\nu)}$ [25–27], where ν is the percolation correlation length exponent [43], which for 2D systems is $\nu = 4/3$.

In another limit case in which a less viscous fluid invades a more viscous liquid at high capillary number, the displacement structure is controlled by viscous forces, which destabilize the invasion front. This viscous fingering regime has been studied both in terms of experiments [14,18,44] and numerical simulations [9,17,45].

The effect of gravity has been studied for sufficiently low capillary numbers in both two and three dimensions [25,27,29,46], but what happens in the crossover regime where gravity, capillary forces and viscous forces all are significant has with the exception of reservoir scale simulations [7,39] not been studied. This crossover regime is what we are addressing in the following discussion.

A. Study of a stable configuration

1. Evolution of the pressure

We consider the situation where the front width reaches a limit value after a certain time, and only exhibits small fluctuations around this value afterward (i.e., stable fronts). For constant flow rate the mean position of the front along the z direction, z_f ($z=0$ at the outlet), would depend linearly on time, with a rate that is imposed by the withdrawal rate and the rate of cluster trapping. We assume that the viscous pressure gradient inside the model can be considered as the sum of an average uniform gradient and of local time-varying fluctuations, where the former term is given by the Darcy law: $|\overline{\nabla P}| = \mu v/\kappa$. As a result, the pressure at the outlet of the model fluctuates around a value given by the relation

$$\overline{P} = P_0 + (\rho g - \mu v/\kappa) z_f(t), \tag{4}$$

where P_0 is the pressure in the nonwetting fluid (air), ρ is the density of the defending fluid, μ is the viscosity of the defending fluid, v is the Darcy velocity, and κ is the model permeability. Therefore, under these assumptions the pressure P recorded at the model outlet as a function of time fluctuates around a linear trend, the slope of which is negative and proportional to $\rho g - \mu v/\kappa$. Note that such a linear dependence of the outlet pressure is only expected for stable fronts. The conditions, in which these conditions are met, are explicited in Sec. III C.

2. Scaling of the front width

The following arguments follow the lines of [25,26,30]. Consider two different pores along the invasion front, labeled A and B and separated by a distance ξ along the z direction (see Fig. 4). If the density and viscosity of the invading nonwetting fluid (air) are negligible, the pressure in the invading nonwetting fluid is constant and in the following we use this as our reference pressure $P_{NW} = 0$. The capillary pressure over pore A is denoted P_A. If we further assume that the viscous field in the defending wetting fluid along the front can be described by Darcy's law, the capillary pressure over pore B, P_B, can be written as the sum of hydrostatic and viscous pressure differences:

$$P_B = P_A + \rho g \xi - \frac{v\mu}{\kappa}\ \xi. \tag{5}$$

The pore throats in the porous medium have widths that are spatially uncorrelated. Each pore throat exhibits a capillary threshold pressure P_t which is the minimum capillary pressure needed for the interface to penetrate the pore throat. For a throat with a meniscus at capillary pressure P_c, the

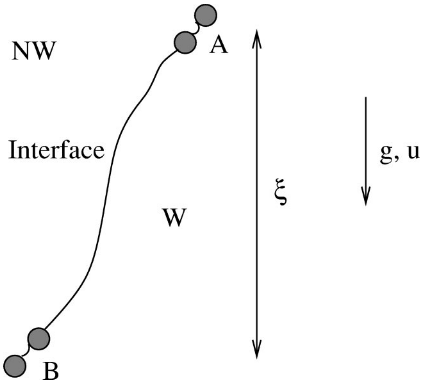

FIG. 4. Sketch of a section of the front including two pores separated by a vertical distance ξ. The capillary pressure over the pore labeled *A* is assumed to be the critical percolation threshold pressure P_C. Assuming stable displacement, we can calculate the pressure at pore *B*.

criterion for invasion is $P_c > P_t$. The randomness of the porous medium gives a distribution $N(P_t)$ for the capillary threshold pressure.

Let us now consider an arbitrary throat in the medium and assume it has a meniscus with capillary pressure P_c. The probability p that this throat will be invaded is

$$p = p^* + \int_{P^*}^{P_c} N(P_t)\,dP_t, \qquad (6)$$

where p^* is the occupation probability at the percolation capillary pressure P^* for a flat model. P^* would then be the lowest capillary pressure needed to produce a percolating cluster of invading fluid. Taylor-expanding $N(P_t)$ around P^* we get

$$N(P_t) = N(P^*) + N'(P^*)(P_t - P^*) + \cdots$$

and to the lowest order in $(P_t - P^*)$ Eq. (6) becomes

$$p - p^* = N(P^*)(P_c - P^*). \qquad (7)$$

If we now let the capillary pressure over pore *A* in Eq. (5) be the percolation threshold capillary pressure P^*, we can use Eq. (5) to rewrite Eq. (7) as

$$p - p^* = N(P^*)\left(\rho g \xi - \frac{v\mu}{\kappa}\xi\right). \qquad (8)$$

Assuming that $N(P_t)$ varies slowly around P^*, we can estimate $N(P^*) = 1/W_t$ [30], where W_t is the width of the normalized capillary threshold pressure distribution $N(P_t)$. With this assumption, Eq. (8) can be rewritten as

$$p - p^* = \frac{\xi}{a} F, \qquad (9)$$

where the dimensionless *generalized fluctuation number F* [30] has been introduced:

$$F = \frac{\rho g a - \dfrac{v\mu a}{\kappa}}{W_t}. \qquad (10)$$

The generalized fluctuation number F quantifies the ratio between the average pressure drop over pores and the fluctuations in capillary threshold pressures in the porous medium. It can be further related to the previously defined Bond and capillary numbers according to

$$B_o - C_a = \frac{a}{\gamma}\; W_t F. \qquad (11)$$

For convenience we define a generalized bond number B_o^* as

$$B_o^* = B_o - C_a. \qquad (12)$$

The length ξ is assumed now to be the correlation length of percolation clusters. Since the linear size of the largest trapped clusters of wetting fluid is limited by the front width w [25,26,40,47], the correlation length is related to the front width in our problem as: $w = \xi/a$. From percolation theory we know [43,47] that

$$A\,\frac{\xi}{a} = (p - p^*)^{-\nu}, \qquad (13)$$

where ν is the correlation length exponent and A is a constant of order unity [26,48]. This scaling relation combined with Eq. (9) yields

$$Aw = A\,\frac{\xi}{a} = \left(\frac{\xi}{a}\right)^{-\nu} F^{-\nu}, \qquad (14)$$

which leads to the following scaling relation for the front width w:

$$w \sim F^{-\nu/(1+\nu)} = \left(\frac{\gamma}{W_t a} B_o^*\right)^{-\nu/(1+\nu)}. \qquad (15)$$

This relation is similar to the one obtained in capillary fingering under gravity [25,30], but in our case the generalized fluctuation number F replaces the ordinary Bond number B_o in the scaling relation (15). It is important to note that F depends on the width of the capillary threshold distribution W_t and that an increase in this width therefore gives an increase in the front width. In the experiments described in this paper, W_t is kept constant. The range of validity of Eq. (15) does not extend to situations where both viscous and gravitational forces exceed the capillary forces on pore scale.

B. Limit of stability

The front width w in the scaling relation in Eq. (15) diverges when the generalized Bond number goes to zero (gravity forces balance viscous forces). This suggests a criterion for finite front widths and thus stable displacement when

$$\rho g - \frac{v\mu}{\kappa} > 0. \tag{16}$$

This is the same stability criterion as derived by Saffman and Taylor [36] for the Hele-Shaw cell, though capillary forces in a Hele-Shaw configuration act at the scale of the system width L (see Fig. 1), while in our porous medium they act at the pore scale a, which is much smaller than L. Section IV E addresses in more detail the differences between the mechanisms of the instability in our model and in a Hele-Shaw cell.

C. Unstable displacement

Slow buoyancy driven unstable displacement has been studied in both two and three dimensions [27,31,32,49]. In this slow regime, string (finger) like structures develop. Their characteristic width w_f was found to scale with the Bond number in a similar fashion as the width of stable fronts:

$$w_f \sim B_o^{-\nu/(1+\nu)}. \tag{17}$$

From these results on buoyancy driven unstable systems we might conjecture that the above equation can be extended in the unstable case to include viscous effect, by replacing in Eq. (17) B_o with $-B_o^*$:

$$w_f \sim (-B_o^*)^{-\nu/(1+\nu)}. \tag{18}$$

An experimental verification of this conjecture is the purpose of ongoing work.

IV. RESULTS

With the setup described in Sec. II A, four main series of experiments were performed, corresponding to a total of 58 experiments: three series at constant capillary number $C_a \simeq 82\times10^{-3}$, 130×10^{-3}, and 190×10^{-3}, and one series at constant Bond number $B_o \simeq 0.155$. Table I summarizes the experimental conditions for all experiments: inclination angle α and withdrawal rate Q, and the corresponding capillary number C_a, Bond number B_o, and generalized Bond number B_o^*. The experiments are numbered by decreasing B_o^*.

A. Observations of the displacement structure when varying B_o^*

Figure 5 shows the pictures of experiments for various capillary numbers and Bond numbers. The pictures shown here correspond to experiments labeled 4, 8, 13, 17, 22, 24, 25, 28, 29, 31, 46, 49, 50, 58 in Table I, from top to bottom and from left to right, respectively. Each column of the figure corresponds to the same capillary number C_a, that is, to the same withdrawal speed applied during the experiment. The withdrawal rates in question are all large enough for the system to exhibit viscous fingering at zero inclination angle. Each line of the figure corresponds to the same generalized Bond number $B_o^* = B_o - C_a$. The maximum accessible Bond number is related to the maximum inclination angle possible with the setup (around 55°). As a consequence, the maximum accessible B_o^* for a given capillary number decreases with C_a, which explains why the highest values of B_o^* investigated here could not be reached for all values of C_a.

When increasing gravity for a given withdrawal speed (thus, following a column in Fig. 5 from bottom to top), the displacement front is observed to evolve from narrow branched fingers to a nearly flat geometry, if the generalized Bond number B_o^* can be increased enough. Thus, viscous effects are responsible for a fingering of the displacement structure that can be stabilized by gravity. The similarity between all pictures on a given line of Fig. 5 suggests that the generalized Bond number is the controlling parameter for the process. This is consistent with relation (15), which will be discussed further in Sec. IV D.

Front destabilization at large withdrawal speed and low gravity appears more clearly in Fig. 6, which looks alike Fig. 5, except that each picture represents the whole dynamics of an experiment. Indeed, a gray level map displays the evolution of the displacement front with time. Time is the vertical descending coordinate, and each horizontal line on a map is a representation of the front at a given time. The coordinate along the t-line is the horizontal coordinate, x. The gray level at a given x along a given t-line corresponds to the difference between the position along z of the most advanced front point at horizontal position x and the mean front advancement along z. A constant gray level along a horizontal line means that the front is flat. Large variations of the gray levels along the line mean that some parts of the front (corresponding to dark shadings) are left far behind others (corresponding to light shadings). Thus, front destabilization appears as an increase of the roughness of the gray level map from the top to the bottom of the figure. Light shaded structures correspond to fingers development. These structures can widen as a result of the branching of the fingers, at low B_o^*. The same gray scale has been used throughout all pictures, which allows us to compare the importance of the fingering process in the various experiments. Pictures with homogeneous and small amplitude roughness correspond to experiments with a stabilized front. The two experiments with $B_o^* > 0$ fulfill this criterion. The intermittency of the dynamics for stable displacement is visible: a finger stops growing after a while, because its length has reached a value that causes gravity to stabilize it; then another finger grows, or the slow part of the front catches up fingers. As B_o^* is decreased below 0, gravity is not sufficient to prevent the fingers from growing forever, and, subsequently, to keep the front total vertical extent around a fixed value. This fingering becomes more important as B_o^* is further decreased. Thus, the crossover for the viscous instability in the presence of gravity seems to occur around $B_o^* = 0$, in good consistency with the theory exposed in Sec. III.

B. Transition from stable to unstable drainage

The destabilization of the front for negative values of B_o^* clearly appears in Fig. 7(a), where the maximal extension of the front along the direction of displacement (z), Δz, is plotted as a function of time normalized by the time at breakthrough, for experiments at C_a around 0.08. The *maximal*

TABLE I. Summary of the inclination angles and withdrawal rates used for each of the 58 experiments. The corresponding characteristic numbers C_a, B_o, and B_o^* are also given. Depending on the withdrawal rate, the uncertainty on C_a and, consequently, on B_o^*, not shown in this table, ranges between 0.009 and 0.025.

Index	1	2	3	4	5	6	7	8	9	10	11	12
α (deg)	54.9	54.9	54.9	54.7	54.9	45.0	54.2	35.7	54.9	30.2	54.9	45.0
Q(ml/min)	0.040	0.480	0.710	1.000	1.280	0.990	1.500	0.990	1.750	0.990	1.740	1.460
B_o	0.155	0.155	0.155	0.154	0.155	0.134	0.153	0.110	0.155	0.095	0.155	0.134
C_a	0.0032	0.0389	0.0581	0.0826	0.0988	0.0787	0.1193	0.0825	0.1351	0.0779	0.1424	0.1341
B_o^*	0.1516	0.1159	0.0967	0.0719	0.0560	0.0551	0.0342	0.0279	0.0198	0.0173	0.0125	−0.0003
Index	13	14	15	16	17	18	19	20	21	22	23	24
α (deg)	24.9	39.9	22.6	54.9	39.9	31.1	19.9	33.1	37.1	17.4	34.9	30.0
Q(ml/min)	0.980	1.480	1.000	2.260	1.540	1.480	1.030	1.480	1.530	1.000	1.510	1.450
B_o	0.080	0.121	0.073	0.155	0.121	0.098	0.064	0.103	0.114	0.057	0.108	0.095
C_a	0.0809	0.1245	0.0787	0.1622	0.1296	0.1142	0.0811	0.1211	0.1358	0.0803	0.1329	0.1231
B_o^*	−0.0013	−0.0031	−0.0060	−0.0074	−0.0082	−0.0165	−0.0167	−0.0177	−0.0217	−0.0237	−0.0246	−0.0285
Index	25	26	27	28	29	30	31	32	33	34	35	36
α (deg)	50.2	48.1	15.0	12.5	27.0	28.9	44.9	48.1	26.8	54.7	54.9	54.9
Q(ml/min)	2.020	2.000	1.040	1.000	1.480	1.500	2.020	2.060	1.610	2.070	2.520	2.270
B_o	0.145	0.141	0.049	0.041	0.086	0.091	0.134	0.141	0.085	0.154	0.155	0.155
C_a	0.1778	0.1745	0.0859	0.0787	0.1257	0.1332	0.1778	0.1860	0.1330	0.2029	0.2042	0.2050
B_o^*	−0.0324	−0.0336	−0.0369	−0.0378	−0.0397	−0.0417	−0.0442	−0.0452	−0.0476	−0.0485	−0.0494	−0.0502
Index	37	38	39	40	41	42	43	44	45	46	47	48
α (deg)	44.9	20.3	10.0	44.9	44.9	43.7	5.0	14.9	10.0	0.0	35.6	28.1
Q(ml/min)	2.050	1.470	1.000	1.960	2.000	2.000	0.990	1.460	1.510	1.020	2.200	2.000
B_o	0.134	0.066	0.033	0.134	0.134	0.131	0.016	0.049	0.033	0.000	0.110	0.089
C_a	0.1867	0.1191	0.0880	0.1891	0.1961	0.1945	0.0841	0.1262	0.1235	0.0961	0.2072	0.1899
B_o^*	−0.0531	−0.0535	−0.0551	−0.0555	−0.0625	−0.0638	−0.0676	−0.0776	−0.0907	−0.0961	−0.0970	−0.1008
Index	49	50	51	52	53	54	55	56	57	58		
α (deg)	5.2	21.1	15.0	0.0	0.0	54.7	15.0	9.3	32.3	0.1		
Q(ml/min)	1.490	1.970	1.950	1.470	1.470	2.800	2.000	1.980	2.600	1.970		
B_o	0.017	0.068	0.049	0.000	0.000	0.154	0.049	0.031	0.101	0.000		
C_a	0.1208	0.1779	0.1626	0.1169	0.1169	0.2810	0.1992	0.1819	0.2750	0.1886		
B_o^*	−0.1036	−0.1098	−0.1136	−0.1169	−0.1169	−0.1265	−0.1502	−0.1513	−0.1739	−0.1882		

extension of the front is defined as the maximal vertical distance between two points on the front. At large positive generalized Bond numbers, the front extension rapidly grows to reach a constant plateau. Fluctuations of Δz occur around this average front extension due to the randomness of the medium. As the Bond number is decreased, these fluctuations grow. Viscous fingering features appear: Δz exhibits sudden drops that are characteristic of the merging of two nearby fingers. For negative values of B_o^* in the intermediate regime, the front extension has a growing trend with no saturation and important sudden drops due to finger merging. For large negative values of B_o^* (not shown in Fig. 7), these drops disappear, as a small number of very thin fingers exist, that never merge. The crossover between stable displacement and unbounded fingering appears to occur for a value of the generalized Bond number between -0.006 ± 0.009 and 0.017 ± 0.013, in good consistency with the predicted value for the generalized Bond number at the crossover: $B_o^*=0$.

Also consistent with the predicted crossover is the evolution of the pressure drop across the model. Figure 7(b) shows the evolution of the pressure drop between the front (atmospheric pressure) and the outlet channel of the model during the same experiments as in Fig. 7(a). For stabilized experiments ($B_o^*>0$), it has been predicted to be linearly dependent on time. This can be seen in Fig. 7(b) for the four experiments with stable displacement. For B_o^* close to 0, the pressure drop shows little variations during drainage: gravity exactly balances the mean viscous pressure gradient. When

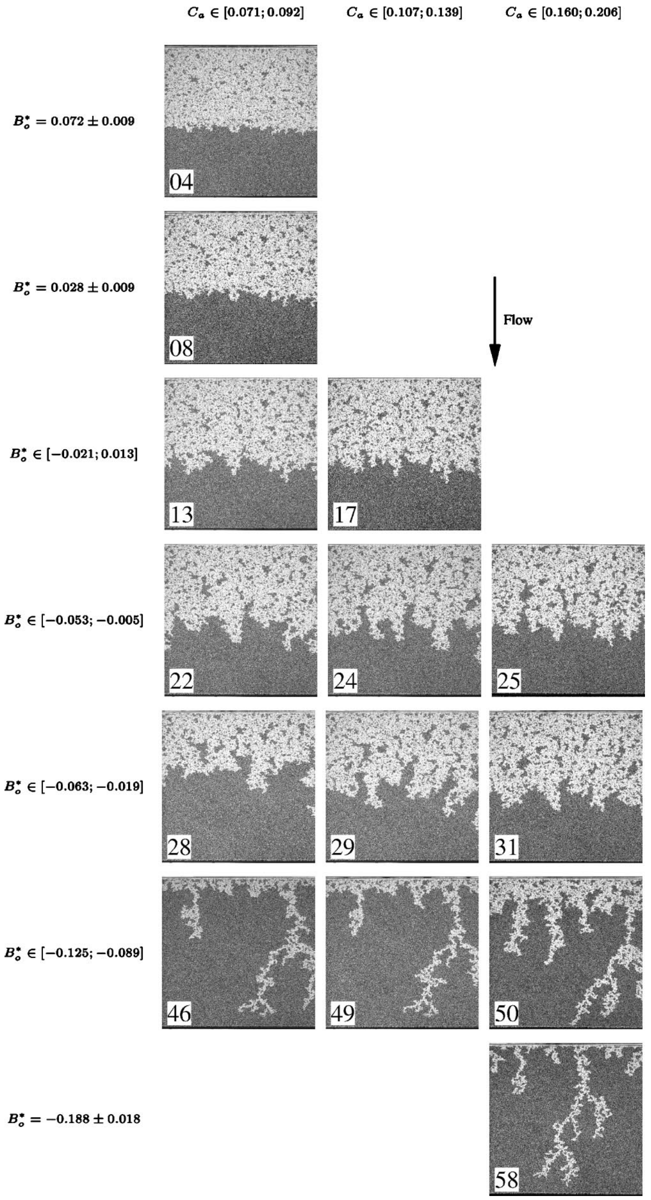

FIG. 5. Pictures of the displacement structure for three series of experiments at capillary number $C_a \simeq 0.081$, 0.123, and 0.183, respectively. The provided ranges include the uncertainty on C_a (and subsequently, on B_o^*) due to that on the viscosity measurements. The pictures represent the whole model (35×35 cm^2). For each series, the displacement structure for an experiment with a generalized Bond number B_o^* around 0.072, 0.028, -0.002, -0.028, -0.041, -0.107, and -0.189 (measured values) is shown. Stabilization of the front is observed for all series when sufficiently increasing B_o^* (bottom to top); the crossover value of B_o^* for stabilization appears to be close to 0. The numbers inserted in the pictures refer to the index in Table I.

the average total pressure gradient turns positive, local effects in the viscous pressure gradient become significant, and nonlinearity appears in the pressure curves, while the trend of the pressure evolution changes from a decreasing to an increasing behavior.

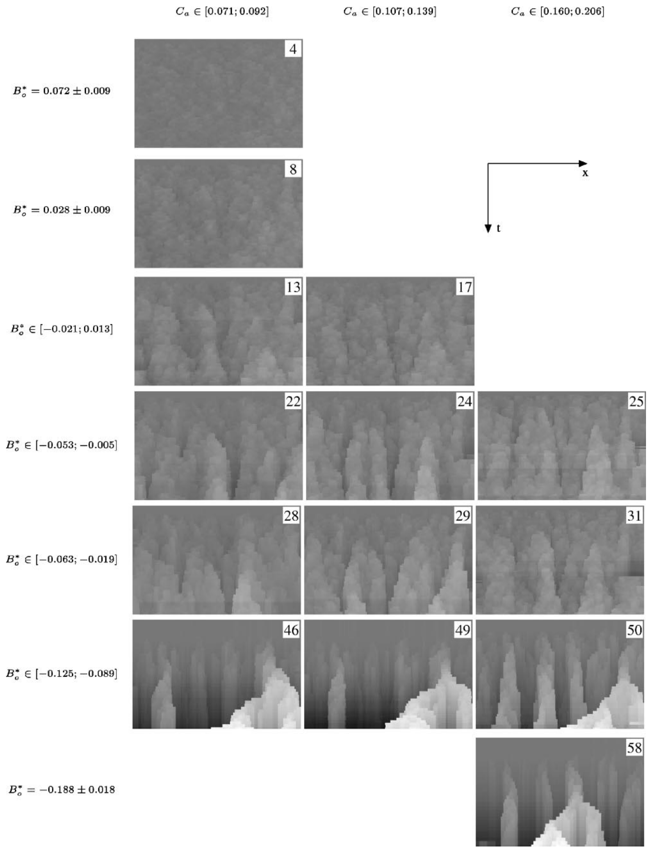

FIG. 6. Evolution of the dynamics of the displacement when varying capillary number C_a and generalized Bond number B_o^*. The values for these numbers are the same as in Fig. 5. Each picture displays the evolution of the displacement front with time. Axes for time and horizontal direction x are shown in the figure. The horizontal size of a picture corresponds to the model width (35 cm). The vertical size corresponds to the time at breakthrough, which depends on the values for C_a and B_o. The gray level is proportional to the advancement of the front point in question with respect to the front mean position. Only the two top pictures, that exhibit a homogeneous roughness of small amplitude, correspond to experiments where the viscous instability is overcome by gravity. The numbers inserted in the pictures refer to the index in Table I.

C. Geometrical properties of the front

The influence on drainage dynamics of the various physical effects involved appears when considering the evolution of the front fractal dimension during an experiment. Indeed, the limit cases in terms of displacement rate are well known. For very slow displacements, viscous effects have little influence on the interface. The displacement front for this capillary fingering regime is analogous to what is observed in inversion percolation. It is fractal, with a fractal dimension 1.33 [13]. In contrast, viscous fingering occurs for very fast displacements, and leads to thin branched fingers that exhibit a fractal structure with a dimension that has been measured to 1.62 ± 0.04 [14].

The fractal dimensions measured in our experiments are consistent with these well-known values. Two families of fronts with behaviors close to gravity stabilized capillary fingering and viscous fingering, respectively, have been ana-

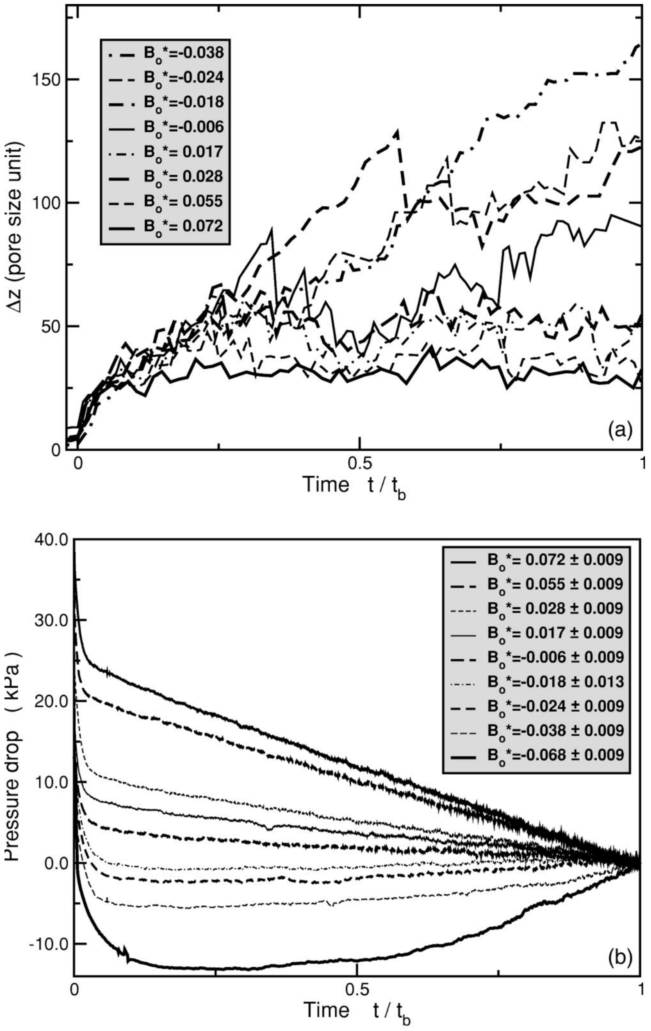

FIG. 7. (a) Evolution of the extension of the front along the direction of displacement (z), Δz, as a function of time normalized by the time at breakthrough. (b) Evolution of the pressure drop between the front and the model outlet channel, as a function of normalized time also. The uncertainties on B_o^* are shown only in (b). Both plots are consistent with the theoretical prediction of a crossover at $B_o^*=0$.

lyzed using both the two-point correlation function and the box-counting algorithm, with consistency. The results of the box-counting method are shown in Fig. 8. The box-counting function for family A (capillary fingering), shown in Fig. 8, has been obtained by averaging over all stabilized fronts in the corresponding experiment. The box-counting function for family B (viscous fingering) is the box-counting function for a sole front because of the unstable growth. At scales smaller than a crossover scale $s<s_c\simeq 20$ pore sizes, fronts A exhibit a regime consistent with that observed for invasion percolation, with a fractal dimension close to 1.3. The crossover scale, s_c, is consistent with the observed front width. At scales larger than s_c, the front is seen as line. Front B displays a fractal structure with a fractal dimension close to 1.6, for scales larger than 2 pore scales and smaller than 80 pore scales. Front B also exhibits some broadening of the fingers at small scales, related to capillary effects. By "small scales," we mean scales smaller than the size of the clusters trapped inside the branched fingers.

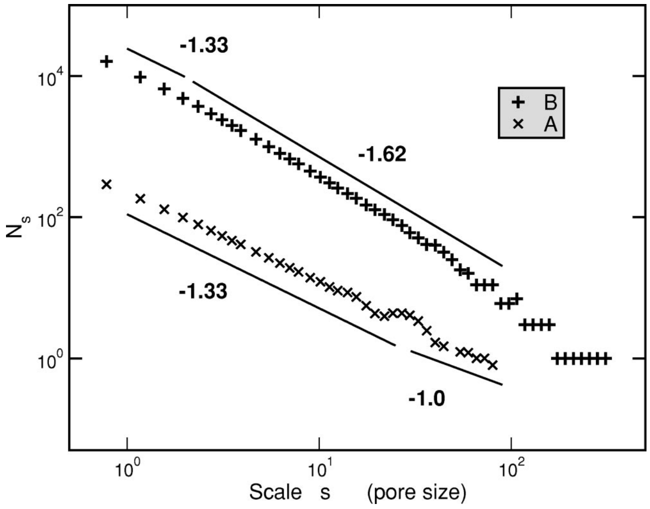

FIG. 8. Characterization of two fronts corresponding respectively to capillary (A) and viscous (B) fingering, using the box-counting method. The front labeled A corresponds to an experiment with a very slow withdrawal rate (0.006 ml/min). Front B corresponds to an experiment with no gravity and a withdrawal rate of 5 ml/min. These two experiments are not referenced in Table I. N_s is the number of boxes of side length s required for entirely covering the front. The observed trends for A and B are consistent with those expected for pure capillary (slope -1.33) and viscous fingering (slope -1.62), respectively.

For the intermediate regimes in which viscous forces and gravity are of the same order of magnitude, parts of the front display fingers controlled by viscous effects. The finger tips progress faster than other parts of the front, which are controlled by the balance between capillary forces and gravity (see Fig. 3). The evolution of the correlation function on the whole range of scales during an experiment gives hints on the dynamics of the displacement process. In Fig. 9(b), density-density correlation functions for a series of experiments in stable regime and corresponding to various values of the generalized Bond number, B_o^*, have been plotted as a function of the scale normalized by the mean front width, w. One front from each of these experiments is shown in Fig. 9(a). They come from seven different experiments in the stable regime with $B_o=0.154$ but with different injection rates. By increasing the injection rate, the pressure gradients in the fluid decrease, which yields a lower B_o^* and therefore a wider front. At the largest speeds the fronts look visually somewhat different from the fronts observed for pure capillary stabilized fingering. The depth of the fjords are typically larger than their width.

The correlation functions in Fig. 9(b) were obtained by averaging over all stable fronts from the experiments in question. The correlation function is divided by $s^{-0.67}$, which is the expected scaling in the capillary fingering regime. The correlation function corresponding to the slowest withdrawal rate (experiment 1) exhibits at small scales a clear horizontal line characteristic for capillary fingering. The horizontal line C is a guide to the eye. At higher injec-

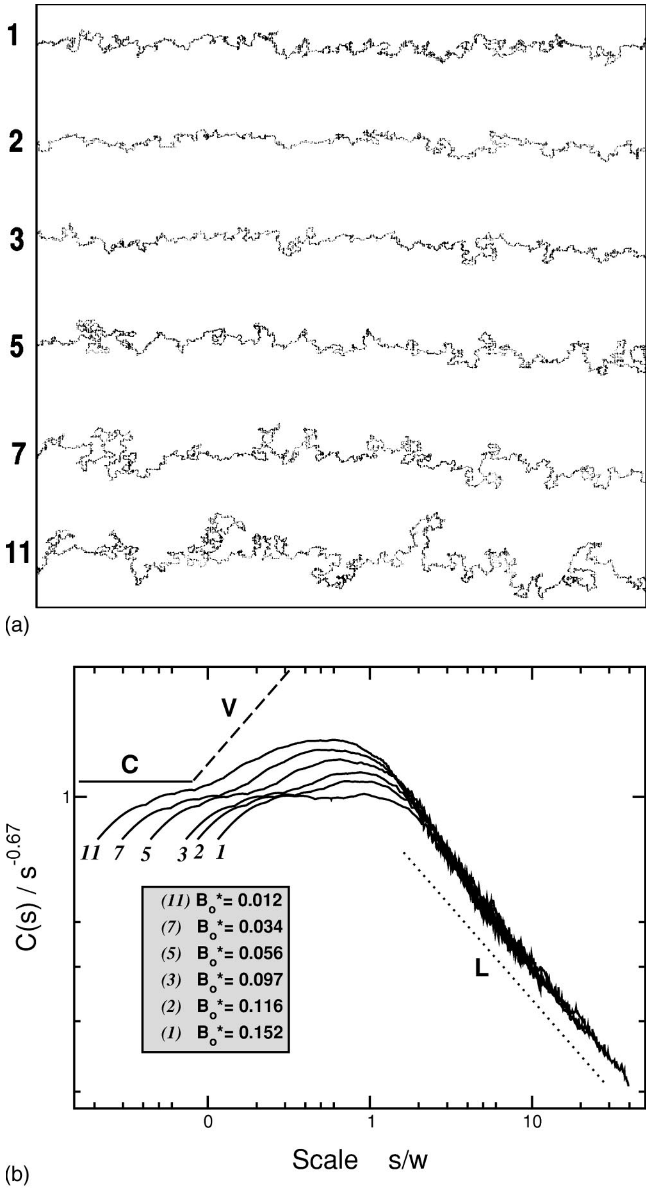

FIG. 9. (a) Fronts taken from experiments at $B_o \simeq 0.154$ and for 6 different displacement rates, all corresponding to positive generalized Bond numbers B_o^* (stable displacement). (b) Corresponding correlation functions for these experiments. Each function has been obtained by averaging over all stable fronts. The scale is normalized by the measured front width, *w*, which, according to relation (15), is expected to scale as $B_o^{*-4/7}$ (see Fig. 10 for a confirmation of this prediction). The horizontal line *C* corresponds to the capillary fingering behavior, the long-dashed line *V* to the pure viscous fingering behavior, and the dotted line *L* to the linear shape of the front. Experiment 1 is close to pure capillary fingering [as exposed in Fig. 8 (case A)]. Due to viscous effects, the dynamics of the displacement is not that of invasion percolation for regimes close to the instability threshold.

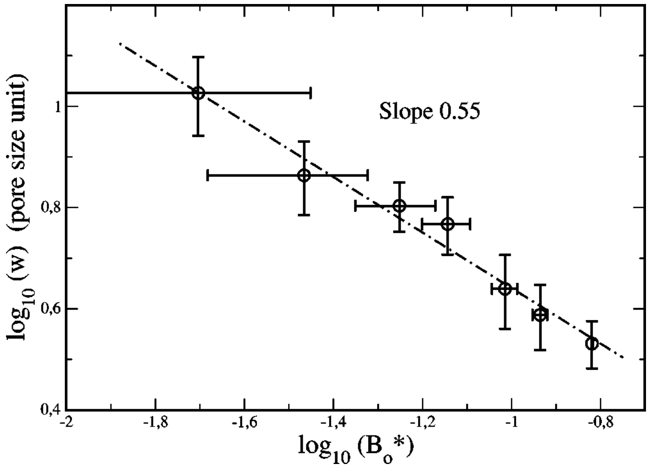

FIG. 10. Scaling of the front width as a function of the generalized Bond number B_o^* for a series of experiments in stable configuration at $B_o \simeq 0.154$. The regression is consistent with a power law with an exponent -0.55, in good agreement with the theoretically predicted relation (15). Vertical error bars represent the uncertainty on the determination of the mean front width for a given experiment. Horizontal error bars are related to the uncertainty in the viscosity measurements.

tion rates the correlation function displays a crossover which becomes more significant as the injection rate is increased. This crossover is the Hallmark of significant viscous effects and is seen as an increase in the effective slope on length scales larger than the initial capillary regime (the part on small length scales with a slope close to zero), but smaller than the front width. It is important to note that all these fronts are in the stable regime. As a guide to the eye we have also plotted the slope 0.3 (see long-dashed line *V*), which is the expected slope for unstable viscous fingers. As seen in the figure, the effective slope observed in the viscous crossover regime is larger than the slope characteristic of pure capillary fingering, but smaller than that characteristic of pure viscous fingering. At scales larger than the width of the fronts, the fronts become effectively linear with a slope corresponding the dotted line *L*, which is the expected result for a linear front.

D. Scaling of the front width for stable displacements

In the case of stable displacement, Eq. (15) predicts a scaling of the front width as a power law of the generalized Bond number, $B_o^* = B_o - C_a$, with an exponent $-\nu/(1+\nu) = -4/7$ (≈ -0.57). Figure 10 shows the evolution of the front width, *w*, as a function of B_o^*, for a series of experiments at Bond number $B_o = 0.154 \pm 0.01$. The experiments in question are indexed 1, 2, 3, 4, 5, 7, and 9 in Table I. The values for the front width have been obtained by averaging over all stabilized fronts from the corresponding experiment. The error bars account for the sensitivity of the time averaging on the choice of the time after which the fronts are supposed to be stabilized. The dependence of *w* on B_o^* is consistent with a power law with an exponent -0.55, in good agreement with the theoretical predictions.

E. Discussion

The viscous instability observed in the present article appears for a magnitude of gravity identical to that of the viscous forces. Such a crossover was also observed by Saffman and Taylor in a Hele-Shaw cell with no porous medium under the same conditions. However, though the forces responsible for the stability or instability of the interface are of identical nature, the resulting displacement processes are significantly different in the two geometries.

The first striking difference lies in the nature of stable displacement in the two configurations. A stable displacement in the Hele-Shaw cell configuration means that the front exhibits no roughness. Observed in the uniformly moving referential attached to its mean position, the front is simply static. In our porous model, in contrast, an initial front roughness appears due to capillary fluctuations; during later stages of the drainage process, this roughness develops due to both local viscous effects and inhomogeneous capillary forces. The resulting displacement front has a significant roughness in the direction of displacement. Observed in the moving frame attached to its mean position, the front is ever changing, but with an amplitude that saturates after a certain time to a value that can be as high as 50 pores scale units. Thus, *stable displacement* consists here in an ongoing competition process where departing viscous fingers are prevented by gravity from developing too much ahead of the front mean position on behalf of other fingers or slowly moving portions of the front. The front width is controlled by the ratio of the mean effective pressure gradient inside the model (i.e., hydrostatic pressure gradient minus viscous pressure gradient) to the inhomogeneous capillary forces. The mean effective pressure gradient is denoted by the generalized Bond number $B_o^* = B_o - C_a$. The inhomogeneous capillary threshold pressures result from the randomness in the porous media. This inhomogeneity could be quantified by the width W_t of the capillary threshold pressure distribution $N(P_t)$. In our case, it is measured to be $W_t \approx \gamma/(4a)$. The ratio between the effective pressure gradient and the fluctuations in capillary threshold pressure distribution is quantified by the dimensionless fluctuation number F defined in Eq. (10). Due to the homogeneity of our porous model, W_t happens to be constant in space. For a medium with a varying pore scale, Eq. (15) indicates possible significant changes in the front width during the displacement process for constant flow rate and gravity component on the model. In the framework of this study, the extensively studied capillary and viscous fingering appear as limit cases where the capillary number, C_a, or Bond number, B_o, respectively, are negligible. The scaling relation obtained for the front width in stable displacement as a function of F, and thus, of B_o^*, is therefore a generalization of that previously obtained for capillary fingering. Indeed, Bond number and generalized Bond number are identical when the capillary number is negligible.

Second, the transition from stable to unstable displacement in our system does not consist of a radical change in the local dynamics of the interface, as for viscous instability observed in a Hele-Shaw cell. For a configuration close to the instability threshold, it is difficult to know, by looking at the local dynamics of the displacement in our experimental model, whether the front amplitude is going to reach a saturation value or whether it is going to grow forever. This is also visible from the large fluctuations in the front width evolution for configurations close to the instability threshold, in Fig. 7: do these large fluctuations diverge or do they oscillate around a constant value? In the case of the Hele-Shaw cell configuration, in contrast, the instability can be inferred as soon as a significant roughness appears in the front. In a sense, the complexity of the porous medium translates into a complexity in the viscous instability.

V. CONCLUSION

We have studied experimentally the displacement of a mixture of glycerol and water by air at constant volumetric flow rate in a synthetic random two-dimensional medium. The experimental setup allowed the tuning of gravity by tilting the setup and of viscous effects by changing the withdrawal rate. The aim of the study was to investigate the crossover regime from capillary fingering to viscous fingering during drainage with gravity. To account for the relative importance of viscous- and gravitational effects during drainage, we have introduced the fluctuation number F which is defined as the ratio of the effective fluid pressure drop (i.e., average hydrostatic pressure drop minus viscous pressure drop) at pore scale to the width of the fluctuations in the threshold capillary pressures. We observe a crossover at $F = 0$ between a configuration where the displacement front keeps a finite extension along the direction of flow ($F > 0$) and a situation where fingers grow ahead of other parts of the front, forever ($F < 0$). Gravity stabilized capillary fingering and pure viscous fingering appear as limit cases where viscous effects or gravity effects, respectively, have little influence on the displacement structure.

In intermediate regimes (F close to 0), the dynamics of the displacement seems to hold features characteristic of invasion percolation (for short length scales of the front) as well as features characteristic of viscosity-controlled fingering. The crossover is smooth and might lead to an apparent misleading dimension of the front in a midrange between capillary regime and viscous fingering dimension. The drainage process is both inhomogeneous in time and space. For positive values of the fluctuation number, the front width has a physical meaning in terms of fluctuations of the front around a mean position that progresses at constant speed. This front width is controlled by viscous effects and scales as a power law of the fluctuation number with an exponent $-4/7$ [see Eq. (15)], a scaling law that we predict theoretically and that is nicely confirmed by the experiments.

For negative values of the fluctuation number, characteristic length scales are difficult to find in the problem. The width of the developing fingers might be a suitable characteristic scale, with a scaling relation identical to Eq. (15) as a function of the generalized Bond number's (or, equivalently, the fluctuation number's) absolute value.

ACKNOWLEDGMENTS

The work was supported by NFR, the Norwegian Research Council, VISTA, the Norwegian Academy of Science and Letters' research program with Statoil and the French/Norwegian collaboration PICS.

[1] F.A.L. Dullien, *Porous Media Fluid Transport and Pore Structure*, 2nd ed. (Academic, San Diego, 1992).

[2] J. Bear, *Dynamics of Fluids in Porous Media* (American Elsevier, New York, 1972).

[3] M. Sahimi, Rev. Mod. Phys. **65**, 1393 (1993).

[4] G.M. Homsy, Annu. Rev. Fluid Mech. **19**, 271 (1987).

[5] P. van Meurs, Trans. AIME **210**, 295 (1957).

[6] A.K. Gustensen and D.H. Rothman, J. Geophys. Res. [Planets] **98**, 6431 (1993).

[7] H.A. Tchelepi and F.M. Orr, SPE Reservoir Eng. **9**, 266 (1994).

[8] I. Ginzburg and P.M. Adler, Transp. Porous Media **20**, 37 (1995).

[9] R. Lenormand, E. Touboul, and C. Zarcone, J. Fluid Mech. **189**, 165 (1988).

[10] D.G. Avraam and A.C. Payatakes, J. Fluid Mech. **293**, 207 (1995).

[11] R. Chandler, J. Koplik, K. Lerman, and J.F. Willemsen, J. Fluid Mech. **119**, 249 (1982).

[12] R. Lenormand and C. Zarcone, Phys. Rev. Lett. **54**, 2226 (1985).

[13] R. Lenormand and C. Zarcone, Transp. Porous Media **4**, 599 (1989).

[14] K.J. Måløy, J. Feder, and T. Jøssang, Phys. Rev. Lett. **55**, 2688 (1985).

[15] O.I. Frette, K.J. Maløy, J. Schmittbuhl, and A. Hansen, Phys. Rev. E **55**, 2969 (1997).

[16] E. Aker, K.J. Måløy, and A. Hansen, Phys. Rev. Lett. **84**, 4589 (2000).

[17] J.-D. Chen and D. Wilkinson, Phys. Rev. Lett. **55**, 1892 (1985).

[18] J. Nittman, Physica A **140**, 124 (1986).

[19] T.A. Witten and L.M. Sander, Phys. Rev. Lett. **47**, 1400 (1981).

[20] T.A. Witten and L.M. Sander, Phys. Rev. B **27**, 5686 (1983).

[21] P. Meakin, Phys. Rev. A **27**, 1495 (1983).

[22] L. Paterson, Phys. Rev. Lett. **52**, 1621 (1984).

[23] E.L. Hinrichsen, K.J. Måløy, J. Feder, and T. Jøssang, J. Phys. A **22**, L271 (1989).

[24] F.A.L. Dullien, Chem. Eng. Technol. **11**, 407 (1988).

[25] A. Birovljev, L. Furuberg, J. Feder, T. Jøssang, K.J. Måløy, and A. Aharony, Phys. Rev. Lett. **67**, 584 (1991).

[26] D. Wilkinson, Phys. Rev. A **30**, 520 (1984).

[27] A. Birovljev, G. Wagner, P. Meakin, J. Feder, and T. Jøssang, Phys. Rev. E **51**, 5911 (1995).

[28] G. Wagner, A. Birovljev, P. Meakin, J. Feder, and T. Jøssang, Phys. Rev. E **55**, 7015 (1997).

[29] E. Clément, C. Baudet, and J.P. Hulin, J. Phys. D **20**, 608 (1987).

[30] H. Auradou, K.J. Måløy, J. Schmittbuhl, A. Hansen, and D. Bideau, Phys. Rev. E **60**, 7224 (1999).

[31] V. Frette, J. Feder, T. Jøssang, and P. Meakin, Phys. Rev. Lett. **68**, 3164 (1992).

[32] P. Meakin, A. Birovljev, V. Frette, J. Feder, and T. Jøssang, Physica A **191**, 227 (1992).

[33] G. Wagner, P. Meakin, J. Feder, and T. Jøssang, Physica A **245**, 217 (1997).

[34] W.B. Heines, J. Agric. Sci. **20**, 97 (1930).

[35] E. Aker, K.J. Måløy, A. Hansen, and S. Basak, Europhys. Lett. **51**, 55 (2000).

[36] P.G. Saffman and G. Taylor, Proc. R. Soc. London, Ser. A **245**, 312 (1958).

[37] A. Vedvik, G. Wagner, U. Oxaal, J. Feder, P. Meakin, and T. Jøssang, Phys. Rev. Lett. **80**, 3065 (1998).

[38] D. Zhou and F.M.J. Orr, In Situ **19**, 249 (1995).

[39] F.J. Fayers, J. Jouaux, and H.A. Tchelepi, In Situ **18**, 79 (1994).

[40] J.F. Gouyet, M. Rosso, and B. Sapoval, Phys. Rev. B **37**, 1832 (1988).

[41] B.B. Mandelbrot, *The Fractal Geometry of Nature* (Freeman, New York, 1982).

[42] G. Wagner, H. Amundsen, U. Oxaal, J. Feder, and T. Jøssang, Pure Appl. Geophys. **157**, 621 (2000).

[43] D. Stauffer and A. Aharony, *Introduction to Percolation Theory*, 2nd ed. (Taylor & Francis, London, 1991).

[44] K.J. Måløy, F. Boger, J. Feder, T. Jøssang, and P. Meakin, Phys. Rev. A **36**, 318 (1987).

[45] E. Aker, K.J. Måløy, A. Hansen, and G.G. Batrouni, Transp. Porous Media **32**, 163 (1998).

[46] M. Chaouche, N. Rakotomalala, D. Salin, B. Xu, and Y.C. Yortsos, Chem. Eng. Sci. **49**, 2447 (1994).

[47] B. Sapoval, M. Rosso, and J.F. Gouyet, J. Phys. (France) Lett. **46**, L149 (1985).

[48] D. Stauffer, Phys. Rep. **54**, 1 (1979).

[49] B. Xu, Y.C. Yortsos, and D. Salin, Phys. Rev. E **57**, 739 (1998).